PHOTOENZYMOLOGY

Asymmetric photoenzymatic incorporation of fluorinated motifs into olefins

Maolin Li[1,2,3], Yujie Yuan[1,2,3], Wesley Harrison[1,2,3], Zhengyi Zhang[1,2,3], Huimin Zhao[1,2,3,4]*

Enzymes capable of assimilating fluorinated feedstocks are scarce. This situation poses a challenge for the biosynthesis of fluorinated compounds used in pharmaceuticals, agrochemicals, and materials. We developed a photoenzymatic hydrofluoroalkylation that integrates fluorinated motifs into olefins. The photoinduced promiscuity of flavin-dependent ene-reductases enables the generation of carbon-centered radicals from iodinated fluoroalkanes, which are directed by the photoenzyme to engage enantioselectively with olefins. This approach facilitates stereocontrol through interaction between a singular fluorinated unit and the enzyme, securing high enantioselectivity at β, γ, or δ positions of fluorinated groups through enzymatic hydrogen atom transfer—a process that is notably challenging with conventional chemocatalysis. This work advances enzymatic strategies for integrating fluorinated chemical feedstocks and opens avenues for asymmetric synthesis of fluorinated compounds.

Fluorine's electronic properties, small size, and lipophilicity have a profound impact on the function of organic molecules, particularly bioactive compounds (*1*, *2*). The introduction of fluorinated motifs can augment a molecule's bioavailability, metabolic stability, and protein interactions, which makes fluorinated compounds integral to both pharmaceutical and agrochemical industries (*3*), representing ~20% of the pharmaceutical market (*4*). Despite the prominence and potential usefulness of fluorinated molecules, the enzyme 5′-fluoro-5′-deoxyadenosine synthetase (FDAS) or fluorinase represents nature's only currently known tool for incorporating fluorine into organic molecules (*5*). FDAS operates through a nucleophilic attack by a fluoride ion on *S*-adenosyl-L-methionine (SAM) (Fig. 1A). Naturally occurring fluorinated products are thus limited to just a few molecules ultimately derived from 5′-deoxy-5′-fluoroadenosine (*6*). To broaden the scope of biocatalytic fluorine chemistry, two primary strategies are currently being pursued (*6*, *7*). The first involves the expansion of the substrate scope of natural fluorinase enzymes through protein engineering, coupled with the modification of biosynthetic pathways to integrate fluorinated building blocks, thereby facilitating precu… directed biosynthesis (*8*–*10*). The second s… egy focuses on developing new enzymatic reactions using fluorinated substrates, aiming to incorporate non-natural fluorinated motifs into existing protein systems (*11*–*16*). Despite notable advancements, these approaches face limitations in substrate scope and efficiency. Additionally, certain fluorinated groups of importance in the pharmaceutical and agrochemical industries, such as fluoroalkyl groups (-CF_3, -CF_2CF_3, etc.), remain underexplored, thus constraining their synthetic applications.

Unlike enzymatic fluorination, the broader field of chemistry brings forth a diverse array of methods to embed fluorine within molecular structures (*17*–*20*). These chemical methods can seamlessly introduce both single fluorine and more sophisticated fluorinated motifs, such as trifluoromethyl, difluoromethyl, oxytrifluoromethyl, and thio-trifluoromethyl motifs. However, achieving high enantioselectivity with fluorinated motifs that are remote to the stereogenic center remains an overwhelming challenge in chemocatalysis (*21*–*23*). This limitation arises from the limited potential of fluorinated motifs to forge strong interactions with

[1]DOE Center for Advanced Bioenergy and Bioproducts Innovation, University of Illinois Urbana-Champaign, Urbana, IL 61801, USA. [2]Department of Chemical and Biomolecular Engineering, University of Illinois Urbana-Champaign, Urbana, IL 61801, USA. [3]Carl Woese Institute for Genomic Biology, University of Illinois Urbana-Champaign, Urbana, IL 61801, USA. [4]NSF Molecular Maker Lab Institute, University of Illinois Urbana-Champaign, Urbana, IL 61801, USA.
*Corresponding author. Email: zhao5@illinois.edu

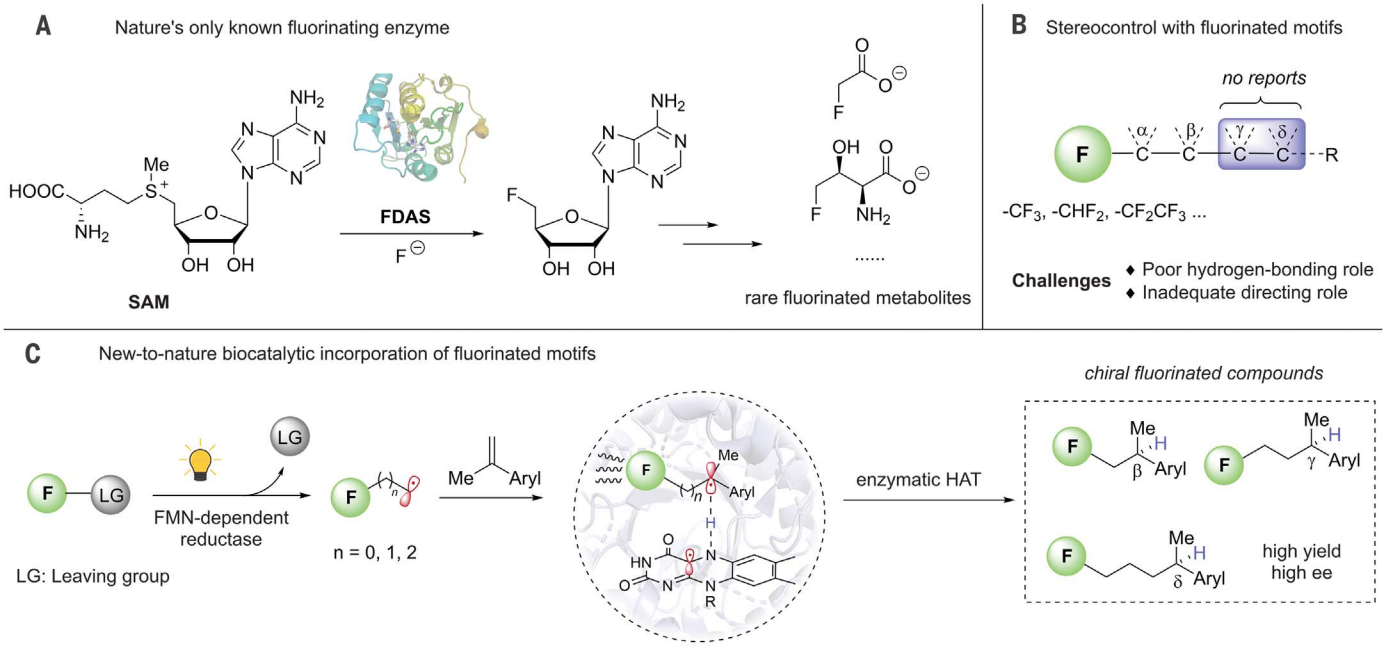

Fig. 1. Enzymatic fluorination: From nature's lone approach to new-to-nature photoenzyme-mediated strategies. (**A**) Reaction scheme of FDAS, nature's singular enzymatic route to use fluorine. (**B**) Challenges in chemocatalysis for achieving stereocontrol with fluorinated motifs. (**C**) Proposed pathway using FMN-dependent reductases for the integration of fluorinated motifs to alkenes and for stereocenter formation through enzymatic HAT. F (in green ring), fluorinated motifs; Me, methyl.

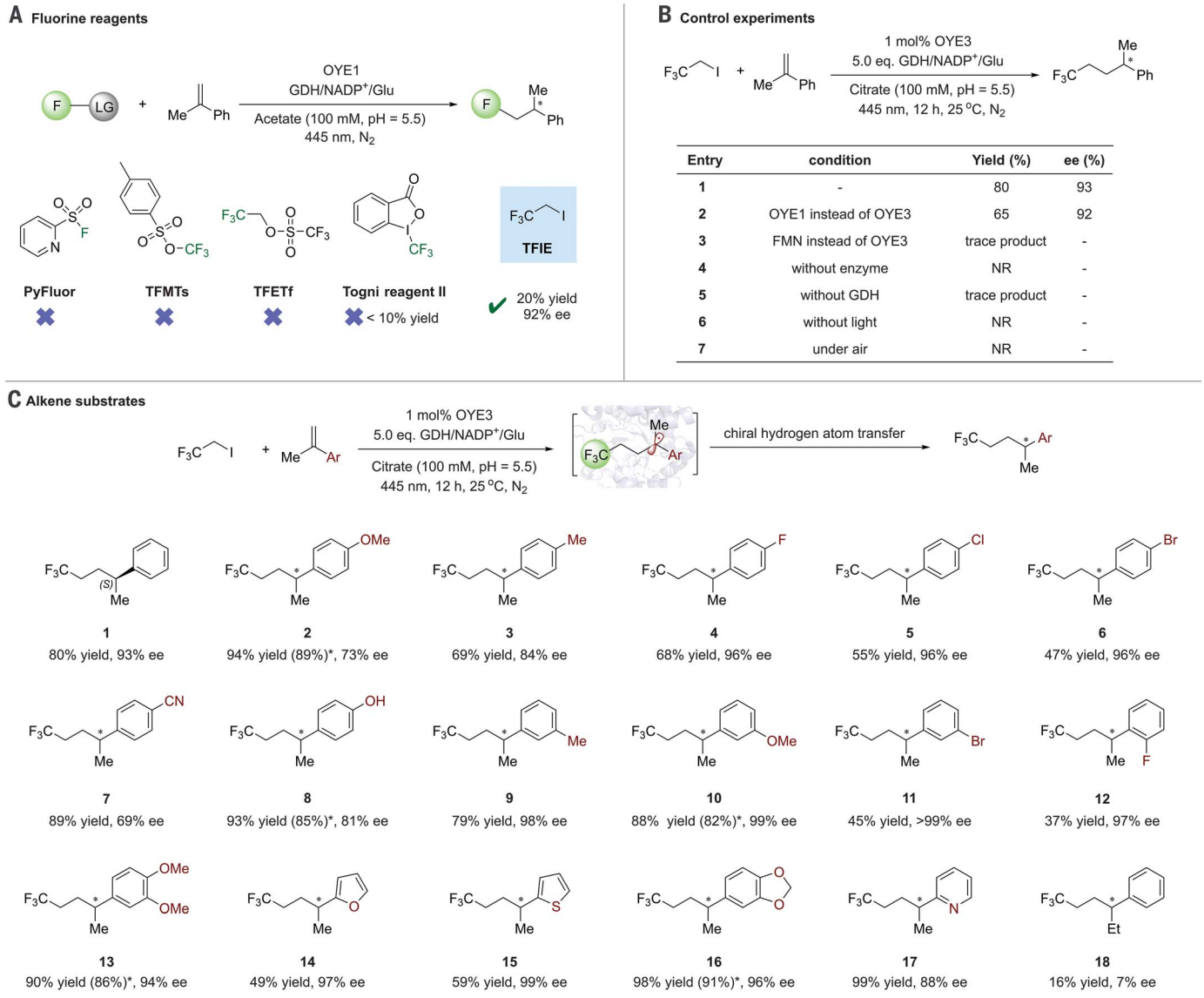

Entry	condition	Yield (%)	ee (%)
1	-	80	93
2	OYE1 instead of OYE3	65	92
3	FMN instead of OYE3	trace product	-
4	without enzyme	NR	-
5	without GDH	trace product	-
6	without light	NR	-
7	under air	NR	-

Fig. 2. Expanding the horizon of asymmetric photoenzymatic catalysis using fluorinated motifs. (**A**) Identification of TFIE as an effective fluorine source using OYE1. (**B**) Optimization and control experiments for superior performance of OYE3 in yield and enantioselectivity. (**C**) Broad substrate adaptability, showcasing the versatility of the enzymatic approach with notable yields and enantioselectivities. Optimal conditions: olefins (4 μmol), TFIE (32 μmol), OYE3 (1 mol % based on olefins), GDH-105 (5 U/ml), $NADP^+$ (1 mol % based on glucose), glucose (20 μmol), and 40 μl of dimethyl sulfoxide (DMSO) as additives in 1 ml (total) of sodium citrate buffer (100 mM, pH = 5.5), 445-nm light-emitting diode (LED), 25°C, and 12 hours. The yield was determined by ^{19}F nuclear magnetic resonance (NMR) spectroscopy with trifluorotoluene as an internal standard. The ee values were determined by chiral gas chromatography (GC). *Isolated yields were determined from 0.06-mmol-scale reactions. Ar, aryl; Et, ethyl; NR, no reaction; eq., equivalent.

catalysts, thereby hindering the propagation of a catalyst's chiral influence to far-flung reaction sites (Fig. 1B). By contrast, thanks to their intricate structures, enzymes might facilitate multifaceted interactions with a fluorinated motif and provide a pervasive chiral environment near the active site, which suggests a promising solution to the above-mentioned challenge (*24*).

The surge of interest in photoenzymes has unlocked pathways for extending enzymatic catalysis into uncharted terrain (*25*–*32*). Key among these are transformations involving flavin mononucleotide (FMN)–dependent reductases, which have demonstrated potential in modulating the enantioselectivity of prochiral carbon-centered radicals through enantioselective hydrogen atom transfer (HAT) (*25*–*28*, *33*–*40*). These enzyme-facilitated reactions typically use photoinduced electron transfer to elevate the substrate to a high-energy and unstable state, followed by the departure of a leaving group (LG), and culminating in radical formation and capture. Building on this foundational knowledge and aiming to fill the long-observed gap of fluorine incorporation in nature, we hypothesize that a carefully chosen fluorine reagent, equipped with a suitable LG, can be used by a photoenzyme to induce the formation of a carbon radical bearing fluorine (Fig. 1C). After the capture of the radical by an olefin, we anticipate achieving chiral control over the remote stereocenters of a singular fluorinated unit through enzymatic HAT. This approach offers the tantalizing prospect of generating an array of fluorinated entities adorned with elusive remote β-, γ-, and δ-stereocenters—a feat challenging in conventional synthesis.

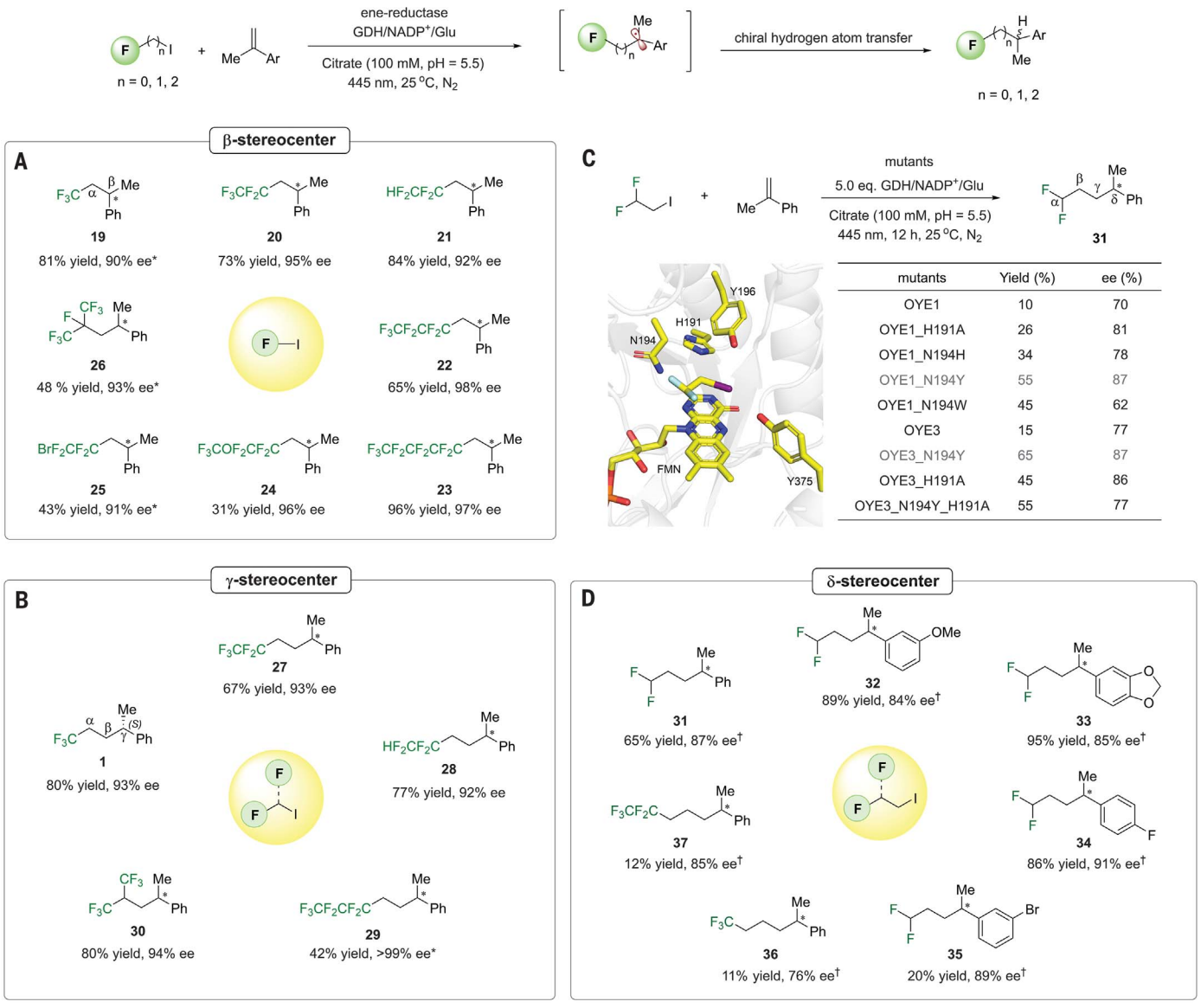

mutants	Yield (%)	ee (%)
OYE1	10	70
OYE1_H191A	26	81
OYE1_N194H	34	78
OYE1_N194Y	55	87
OYE1_N194W	45	62
OYE3	15	77
OYE3_N194Y	65	87
OYE3_H191A	45	86
OYE3_N194Y_H191A	55	77

Fig. 3. Enzymatic exploration of stereocontrolled fluorinated motifs using diverse fluorine reagents. (**A**) Achievements in β-stereocenter construction using perfluoroiodoalkane. (**B**) Results from γ-stereocenter construction optimization using polyfluoroalkane methylene iodide reagents. (**C**) Modeled structure using AutoDock Vina, shown in lowest-energy docking pose, accompanied by the results from δ-stereocenter construction efforts. (**D**) Overview of differential reactivity experiments with varied substrates, emphasizing the potential even with challenging substrates. Optimal reaction conditions: olefins (4 μmol), fluorine reagents (32 μmol), OYE3 (1 mol % based on olefins), GDH-105 (5 U/ml), $NADP^+$ (1 mol % based on glucose), glucose (20 μmol), and 40 μl of DMSO as additives in 1 ml (total) of sodium citrate buffer (100 mM, pH = 5.5), 445-nm LED, 25°C, and 12 hours. The yield was determined by ^{19}F NMR spectroscopy with trifluorotoluene as an internal standard. The ee values were determined by chiral GC or high-performance liquid chromatography (HPLC). *OYE1 (1 mol %). †OYE3_N194Y (1 mol %). Single-letter abbreviations for the amino acid residues are as follows: A, Ala; C, Cys; D, Asp; E, Glu; F, Phe; G, Gly; H, His; I, Ile; K, Lys; L, Leu; M, Met; N, Asn; P, Pro; Q, Gln; R, Arg; S, Ser; T, Thr; V, Val; W, Trp; and Y, Tyr.

Optimization and scope of photoenzymatic hydrofluoroalkylation

FMN-dependent reductases are naturally predisposed to bind substrates with an abundance of carbonyl, nitrile, and nitro groups (*41*). Recent studies have revealed the promiscuity of these reductases, demonstrating their ability to engage substrates adorned with pyridine (*36*, *37*, *42*) or sulfonyl motifs (*33*, *38*, *39*) in photoenzymatic catalysis. Leveraging this promiscuity, we investigated fluorine sources that could be compatible with flavin-dependent ene-reductases. Using the old yellow enzyme 1 (OYE1) from *Saccharomyces pastorianus* as a catalyst and α-methyl styrene as the radical acceptor, we conducted preliminary screenings with some fluorine reagents under blue light. These screenings also used the catalytic regeneration of NADPH (the reduced form of $NADP^+$), mediated by the glucose dehydrogenase (GDH)–nicotinamide adenine dinucleotide phosphate ($NADP^+$)–glucose (Glu) system (Fig. 2A). Typical fluorine agents such as PyFluor, trifluoromethyl tosylate (TFMTs), and trifluoroethyl triflate (TFETf) exhibited no reactivity, but the Togni reagent II showed marginal success with <10% yield. We were intrigued to discover trifluoroiodoethane (TFIE) as an effective fluorine source, producing a γ–chiral center–enriched product in 20% yield and

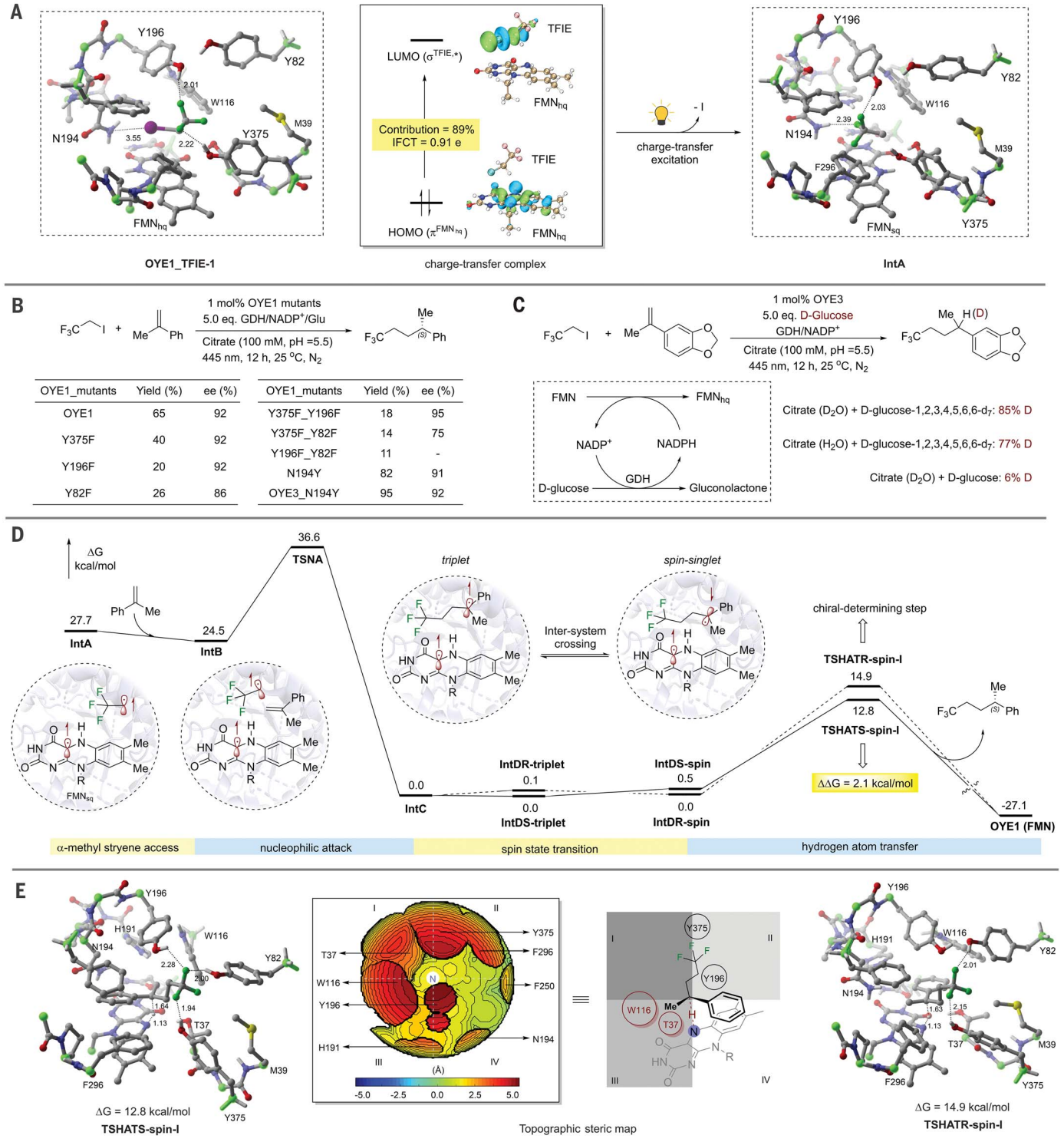

OYE1_mutants	Yield (%)	ee (%)
OYE1	65	92
Y375F	40	92
Y196F	20	92
Y82F	26	86

OYE1_mutants	Yield (%)	ee (%)
Y375F_Y196F	18	95
Y375F_Y82F	14	75
Y196F_Y82F	11	-
N194Y	82	91
OYE3_N194Y	95	92

Fig. 4. Computational and experimental exploration of the reaction mechanism and enantioselectivity. (**A**) Depiction of the initial photochemical reactions leading to the formation of the trifluoroethyl radical and FMN_{sq}. Geometry optimizations were maintained for specific atoms, marked in green, to stabilize the model during simulations. Color coding within the molecular orbital diagrams illustrates the charge transfer: green and blue denote positive and negative orbital phases, respectively. (**B**) Comprehensive evaluation of the effects of mutagenesis on critical amino acids, showcasing their specific roles in the catalytic efficiency. (**C**) Illustration of the cofactor recycling mechanism complemented by deuterium labeling results to trace the reaction pathways and intermediate states. (**D**) Detailed Gibbs energy landscape for the nucleophilic attack step and HAT processes. Computational settings used include um062x-D3/def2tzvpp (SMD, ε = 4.0) // ub3lyp-D3BJ/def2svp (gas), with a comparative analysis of Gibbs free energies relative to **IntC**. (**E**) Topographic steric maps within the OYE1's active site and optimal transition structures for *R* and *S* products. Fixed atoms are highlighted in green.

92% enantioselective excess (ee). In light of the reported reaction with the alkyl iodide in asymmetric reductive cyclization (*43*), we viewed the success of the fluoroalkyl iodide as a starting point toward achieving photoenzymatic asymmetric incorporation of fluorinated motifs and sought to enhance the efficiency of this fluorine reagent through optimization.

Through subsequent evaluations (tables S1 to S6), encompassing various flavin-dependent reductases, ranges of visible light, additives, and solvents, we identified the wild-type old yellow enzyme 3 (OYE3) as the optimal catalyst to furnish the desired product in high yield (80%) with excellent enantioselectivity (93% ee) (Fig. 2B). In comparison, OYE1 rendered the product with a 65% yield and 92% ee under the same conditions. Enzyme, light, and GDH were indispensable for the reaction, as was isolation from oxygen. To demonstrate the scope of trifluoroethyl incorporation, we used various α-methyl vinyl arenes for the reaction with TFIE (Fig. 2C). We achieved moderate to high yields (37 to 99%) with commendable enantioselectivities (69 to 99% ee) (compounds **1** to **13**) for substrates with diverse substituents. Additionally, vinyl arenes, such as furan, thiophene, benzodioxol, and pyridine, were compatible, showing high yields (49 to 99%) and enantioselectivities (88 to 99% ee) (compounds **14** to **17**). We observed that electron-rich alkenes are more efficient because of the affinity of the electron-deficient trifluoroethyl radical toward an electron-rich π system. There is a drop in yield and selectivity with α-ethyl styrene (**18**), which suggests that the active site's efficiency is influenced by steric hindrance from α-alkyl substitutions.

Expansion of scope to various fluoroalkyl groups

We next broadened the enzymatic strategy to encompass a diverse range of fluorine reagents. We first used perfluoroiodoalkane for β-stereocenter construction, producing products (**19** to **26**) with yields of 31 to 84% and enantioselectivities ranging from 90 to 98% ee (Fig. 3A). This approach seamlessly integrated perfluoroalkanes into alkenes. We then applied polyfluorinated methylene iodide reagents to scope the photoenzymatic system for γ-stereocenter construction, yielding fluorinated products (**27** to **30**) with outcomes ranging from 42 to 80% in yield and 92 to 99% ee (Fig. 3B). By adding two methylene spacers between the fluorinated segment and iodine, fluorinated compounds with δ–stereogenic centers were synthesized. However, wild-type OYE1 and OYE3 displayed limited effectiveness, achieving only low yields with around 70% ee (**31**; Fig. 3C). This was attributed to two primary factors: The reduced number of fluorine atoms diminishes interaction with the enzyme, and the increased distance from the fluorinated group to the radical center decreases the radical's nucleophilicity. To address this limitation, we performed targeted mutagenesis on OYE1 and OYE3 using 1,1-difluoro-2-iodoethane and α-methyl styrene as substrates. We docked 1,1-difluoro-2-iodoethane into OYE1 [Protein Data Bank (PDB) ID: 3tx9] (Fig. 3C) and identified putative active-site amino acid residues in the lowest-energy conformation (*44*). Mutagenesis of H191 to alanine augmented reactivity moderately, whereas increasing the size of the N194 side chain substantially improved yield and ee. The OYE3_N194Y variant further optimized the yield to 65% while maintaining 87% ee. Further testing with α-methyl vinyl arenes and 1,1-difluoro-2-iodoethane, along with other advanced substrates 1,1,1-trifluoro-3-iodopropane and 1,1,1,2,2-pentafluoro-4-iodobutane, produced compounds **32** to **37** (Fig. 3D), with a range of yield and ee values.

Mechanistic studies

To study the reaction mechanism, we used a combination of molecular docking and cluster modeling (*45*, *46*) techniques (fig. S1). Using the x-ray crystallographic structure of OYE1 (PDB: 3tx9), we mapped potential conformations of TFIE within the enzyme's active site using AutoDock (*44*). Key amino acid residues proximal to the substrate were identified, each playing a pivotal role in sculpting an open pocket in synergy with flavin hydroquinone (FMN_{hq}) (fig. S2). Through an independent gradient model (IGM) (*47*, *48*), we discerned crucial interactions in the most favorable complex **OYE1_TFIE-1**. Hydrogen bonds were formed by tyrosine residues (Y196 and Y375) with the fluorinated motif and were complemented by van der Waals and a weak halogen bond interaction (Fig. 4A and fig. S3). Time-dependent density functional theory (TDDFT) calculations on the charge-transfer (CT) complex (**OYE1_TFIE-1**) highlighted the role of both the highest occupied molecular orbital (HOMO) and the lowest unoccupied molecular orbital (LUMO), accounting for 89% contribution in the CT excitation (*47*). The interfragment charge-transfer (IFCT) method, based on Multiwfn (*47*), indicated electron transfer of 0.91 electrons from FMN_{hq} to TFIE upon absorption. This CT event paves the way for substrate deiodination and formation of the diradical intermediate **IntA**, which forms interactions between the trifluoromethyl and Y196 and N194 side chains (fig. S4). To validate the computational findings on enzyme-substrate binding, we mutated key tyrosine residues (Y375, Y196, and Y82) to phenylalanine. A decline in activity was observed with fewer tyrosine residues (Fig. 4B). The OYE1_N194Y mutation, shown previously to have improved δ-stereocontrol, enhanced the reaction's yield to 82% with 91% ee. Using OYE3_N194Y as the catalyst almost achieved an equimolar target product yield. These findings underscore the critical role of tyrosine residues in mediating substrate-enzyme interactions, as predicted by our modeling and calculations.

To elucidate the origins of chiral HAT, we conducted deuterium labeling experiments (Fig. 4C and fig. S5). In the Glu-GDH-$NADP^+$ system, glucose acted as a substrate for GDH, facilitating the conversion of $NADP^+$ to NADPH. This subsequent reduction of FMN to FMN_{hq} took place within the OYE1 system. Using deuterated FMN_{hq}, sourced from D-glucose-1,2,3,4,5,6,6-d_7 in a nondeuterated citrate buffer, resulted in a 77% deuterium labeling at the new stereocenter. By contrast, when using nondeuterated D-glucose in a deuterated citrate buffer, the labeling rate decreased sharply to 6%. Such outcomes suggest that the hydrogen atom of the new stereocenter is primarily sourced from FMN_{hq}. The nucleophilic attack step and HAT step were subsequently probed computationally with diradical **IntA** serving as the initiating intermediate. Unbound α-methyl styrene interacts with the trifluoroethyl radical, producing **IntB**. This intermediate then undergoes a radical attack, resulting in **IntC**, which gains a hydrogen atom from flavin semiquinone (FMN_{sq}) to form the final product (Fig. 4D and fig. S6). The HAT transition state, which involves the combination of two radicals, entails a change in electron spin from a triplet to a singlet state (*49*). Detailed computations for the transition state of HAT yielded more than 40 distinct transition states (tables S7 to S9). The most stable transition state was found to be the spin-singlet, whereas the triplet state had the highest energy. Calculations also showed that **IntC** can transition to **IntDS-triplet** and **IntDR-triplet** forms, which later shift to their respective spin variants for HAT (fig. S7). **TSHATS-spin-I** and **TSHATR-spin-I** had the lowest energy barriers, which suggests their key role in determining enantioselectivity. Consistent with experiments, **TSHATS-spin-I** was more energy efficient by 2.1 kcal/mol compared with **TSHATR-spin-I**, emphasizing a preference for the *S* product (fig. S8).

We characterized the lowest-energy transition states of the primary and secondary enantiomers, which are illustrated in Fig. 4E. To probe the origins of enantioselectivity, we used the SambVca (*50*) tool for generating detailed topographic steric maps centered on the FMN nitrogen atom. These maps revealed a complex three-dimensional landscape of amino acid residues, with zones of substantial steric hindrance highlighted in red. Particularly, regions I and III, influenced by residues T37 and W116, showed pronounced steric hindrance. These steric effects critically affect the substrate orientation relative to the FMN plane during the formation of hydrogen bonds with residues

Y196 and Y375. Such spatial arrangement directs the phenyl group toward region IV—the area with minimal steric interference—and pushes the methyl group into the more congested region III, culminating in the formation of the *S*-configuration of the product. Additional studies involving site-directed mutagenesis of critical residues near the enzyme's active site indicated that reducing steric hindrance at residues W116 and T37 led to a decrease in reaction enantioselectivity. By contrast, alanine substitutions at other residues did not markedly affect the outcome (fig. S9). Our steric hindrance maps for the W116A and T37A mutants demonstrate that lessening steric obstacles contributes to reduced differentiation among steric regions I, III, and IV, diminishing the enzyme's ability to discriminate between the methyl and phenyl groups and thereby lowering the enantioselectivity.

In this study, we address a gap in nature's tool kit by developing FMN-dependent photoenzymes for the asymmetric incorporation of fluorinated motifs into vinyl arenes. By exploiting the reactivity of photoexcited FMN reductases, combined with their ability to generate a constrained environment for HAT, we achieved stereoinduction with fluorinated motifs not possible through chemocatalysis. Computational studies provided insights into the interplay between the enzyme and fluorinated substrates, illuminating the origin of stereoselectivity. This work expands the possibilities for enzymatic fluorine utilization and supplements established methods for precise and selective incorporation of fluorinated motifs in asymmetric synthesis.

REFERENCES AND NOTES

1. E. P. Gillis, K. J. Eastman, M. D. Hill, D. J. Donnelly, N. A. Meanwell, *J. Med. Chem.* **58**, 8315–8359 (2015).
2. N. A. Meanwell, *J. Med. Chem.* **61**, 5822–5880 (2018).
3. J. Wang *et al*., *Chem. Rev.* **114**, 2432–2506 (2014).
4. M. Inoue, Y. Sumii, N. Shibata, *ACS Omega* **5**, 10633–10640 (2020).
5. C. Dong *et al*., *Nature* **427**, 561–565 (2004).
6. D. O'Hagan, H. Deng, *Chem. Rev.* **115**, 634–649 (2015).
7. L. Wu, F. Maglangit, H. Deng, *Curr. Opin. Chem. Biol.* **55**, 119–126 (2020).
8. M. C. Walker, M. C. Y. Chang, *Chem. Soc. Rev.* **43**, 6527–6536 (2014).
9. S. Sirirungruang *et al*., *Nat. Chem. Biol.* **18**, 886–893 (2022).
10. A. Rittner *et al*., *Nat. Chem.* **14**, 1000–1006 (2022).
11. C. L. Windle, A. Berry, A. Nelson, *Curr. Opin. Chem. Biol.* **37**, 33–38 (2017).
12. X. Cheng, L. Ma, *Appl. Microbiol. Biotechnol.* **105**, 8033–8058 (2021).
13. X. Huang *et al*., *ACS Cent. Sci.* **5**, 270–276 (2019).
14. J. Zhang, X. Huang, R. K. Zhang, F. H. Arnold, *J. Am. Chem. Soc.* **141**, 9798–9802 (2019).
15. J. Peng, C. Liao, C. Bauer, F. P. Seebeck, *Angew. Chem. Int. Ed.* **60**, 27178–27183 (2021).
16. D. Nam *et al*., *J. Am. Chem. Soc.* **144**, 2590–2602 (2022).
17. M. G. Campbell, T. Ritter, *Chem. Rev.* **115**, 612–633 (2015).
18. C. Ni, M. Hu, J. Hu, *Chem. Rev.* **115**, 765–825 (2015).
19. C. Ni, J. Hu, *Chem. Soc. Rev.* **45**, 5441–5454 (2016).
20. R. Szpera, D. F. J. Moseley, L. B. Smith, A. J. Sterling, V. Gouverneur, *Angew. Chem. Int. Ed.* **58**, 14824–14848 (2019).
21. Y. Zhu *et al*., *Chem. Rev.* **118**, 3887–3964 (2018).
22. P. H. S. Paioti *et al*., *Angew. Chem. Int. Ed.* **61**, e202208742 (2022).
23. M. Briand, E. Anselmi, G. Dagousset, E. Magnier, *Chem. Rec.* **23**, e202300114 (2023).
24. U. T. Bornscheuer *et al*., *Nature* **485**, 185–194 (2012).
25. W. Harrison, X. Huang, H. Zhao, *Acc. Chem. Res.* **55**, 1087–1096 (2022).
26. M. A. Emmanuel *et al*., *Chem. Rev.* **123**, 5459–5520 (2023).
27. J.-P. Wang, M.-H. Zong, N. Li, *Chem Catal.* 10.1016/j.checat.2024.100933 (2024).
28. H. Fu, T. K. Hyster, *Acc. Chem. Res.* **57**, 1446–1457 (2024).
29. L. Cheng *et al*., *Science* **381**, 444–451 (2023).
30. C. Zhu *et al*., *Angew. Chem. Int. Ed.* **62**, e202311762 (2023).
31. Y. Xu *et al*., *Nature* **625**, 74–78 (2024).
32. S. Ju *et al*., *Nat. Chem.* (2024).
33. X. Chen *et al*., *Angew. Chem. Int. Ed.* **62**, e202218140 (2023).
34. Z. Zhang *et al*., *Nat. Catal.* **6**, 687–694 (2023).
35. B. Zhao *et al*., *Nat. Catal.* **6**, 996–1004 (2023).
36. M. Li, W. Harrison, Z. Zhang, Y. Yuan, H. Zhao, *Nat. Chem.* **16**, 277–284 (2024).
37. S.-Z. Sun *et al*., *Nat. Catal.* **7**, 35–42 (2024).
38. Q. Shi *et al*., *J. Am. Chem. Soc.* **146**, 2748–2756 (2024).
39. L. Jiang *et al*., *ACS Catal.* **14**, 6710–6716 (2024).
40. W. Harrison *et al*., *J. Am. Chem. Soc.* **146**, 10716–10722 (2024).
41. H. S. Toogood, N. S. Scrutton, *ACS Catal.* **8**, 3532–3549 (2019).
42. Y. Nakano *et al*., *Angew. Chem. Int. Ed.* **59**, 10484–10488 (2020).
43. P. D. Clayman, T. K. Hyster, *J. Am. Chem. Soc.* **142**, 15673–15677 (2020).
44. O. Trott, A. J. Olson, *J. Comput. Chem.* **31**, 455–461 (2010).
45. F. Himo, *J. Am. Chem. Soc.* **139**, 6780–6786 (2017).
46. X. Sheng, M. Kazemi, F. Planas, F. Himo, *ACS Catal.* **10**, 6430–6449 (2020).
47. T. Lu, F. Chen, *J. Comput. Chem.* **33**, 580–592 (2012).
48. C. Lefebvre *et al*., *Phys. Chem. Chem. Phys.* **19**, 17928–17936 (2017).
49. C. T. Saouma, J. M. Mayer, *Chem. Sci.* **5**, 21–31 (2014).
50. L. Falivene *et al*., *Nat. Chem.* **11**, 872–879 (2019).
51. M. Li, Y. Yuan, W. Harrison, Z. Zhang, H. Zhao, Photoenzymatic asymmetric incorporation of fluorinated motifs into olefins, Dataset, Dryad (2024); https://doi.org/10.5061/dryad.r2280gbm6.

ACKNOWLEDGMENTS

We acknowledge the Computational Chemistry Commune (http://bbs.keinsci.com/) for their support with the calculations. Our research benefited from the computing resources at Delta, the National Center for Supercomputing Applications, enabled by allocation BIO230016 from the Advanced Cyberinfrastructure Coordination Ecosystem: Services & Support (ACCESS) program, funded by National Science Foundation grant nos. 2138259, 2138286, 2138307, 2137603, and 2138296. The Delta research computing initiative, funded by the National Science Foundation (award OCI 2005572), the State of Illinois, and a partnership between the University of Illinois at Urbana-Champaign and its National Center for Supercomputing Applications, is deeply appreciated. We thank G. Jiang and H. Cui for their invaluable insights and L. T. Burrus and M. C. O'Dell for their organizational assistance during the project. **Funding:** This work was funded by the DOE Center for Advanced Bioenergy and Bioproducts Innovation, under the auspices of the US Department of Energy (DOE), Office of Science, Office of Biological and Environmental Research (award no. DE-SC0018420 to H.Z.). The funders had no role in the study design, data collection and analysis, decision to publish, or preparation of the manuscript. **Author contributions:** The project was coordinated by H.Z., and H.Z. and M.L. jointly conceptualized the project and designed the research experiments. M.L. executed the experiments and computational studies. Y.Y. contributed to the construction of the mutants, and W.H. and Z.Z. were responsible for synthesizing some olefin substrates. **Competing interests:** The authors declare no competing interests. **Data and materials availability:** Coordinate files for the molecular docking and cluster modeling are available on Dryad (*51*). All other data are available in the main text or supplementary materials.

SUPPLEMENTARY MATERIALS

science.org/doi/10.1126/science.adk8464
Materials and Methods
Supplementary Text
Figs. S1 to S10
Tables S1 to S9
References (*52*–*68*)
MDAR Reproducibility Checklist

Submitted 14 September 2023; accepted 5 June 2024
10.1126/science.adk8464